Petroleum Science 23 (2026) 3270–3281

Contents lists available at ScienceDirect

Petroleum Science

journal homepage: www.keaipublishing.com/en/journals/petroleum-science

Original Paper

Efficient P/S and up/down wavefield decomposition in vertical transversely isotropic media and its application in elastic reverse time migration

Wei Wu [a,b], Le-Le Zhang [b,*], Yang Zhao [c], Yang Liu [b], Xiao-Feng Wu [b], Hao-Huan Fu [d]

[a] *Department of Earth System Science, Tsinghua University, Beijing, 100084, China*
[b] *BGP Inc., CNPC, Zhuozhou, 072751, Hebei, China*
[c] *State Key Laboratory of Petroleum Resource and Engineering, and Unconventional Petroleum Research Institute, China University of Petroleum (Beijing), Beijing, 102249, China*
[d] *Tsinghua Shenzhen International Graduate School, Shenzhen, 518055, Guangdong, China*

A R T I C L E I N F O

Article history:
Received 23 August 2025
Received in revised form
19 November 2025
Accepted 20 January 2026
Available online 25 January 2026

Edited by Meng-Jiao Zhou

Keywords:
P/S wavefield decomposition
Up/down going wave separation
Elastic reverse time migration
Anisotropy

A B S T R A C T

Common artifacts existing in anisotropic elastic reverse time migration (ERTM) image are mainly cross-talk artifacts, false images and low-frequency noise. To address these problems, we propose a new elastic wave decomposition approach in vertical transversely isotropic (VTI) media, which decompose original elastic wavefield into up-/down-going P-wave and S-wave components for ameliorating imaging artifacts in ERTM. We first apply a space-domain VTI P/S wave-mode decomposition operator, reducing the cross-talk artifacts of ERTM image. Then, we derive the dispersion relation formulation of P-wave and S-wave which are used to construct Hilbert transformed operators in VTI media. For adapting to complex model, the first-order Taylor expansion around anisotropic parameter is applied to these derived P/S wave Hilbert transformed operators. We therefore present an up/down wavefield separation operator for VTI media that requires solving the wave equation only once, computing both the original wavefield and its Hilbert transform. This up/down going separated operator can be used to suppress false images and low-frequency noise of ERTM images. Finally we embed proposed up/down going wave separation into P/S wave-mode decomposition and develop a new elastic wave decomposing approach, which can efficiently improve the image quality in VTI ERTM. Simple and complex synthetic models demonstrate the effectiveness of our method.

1. Introduction

Compared to acoustic reverse time migration (ARTM), elastic reverse time migration (ERTM) demonstrates superior capabilities in lithology characterization and complex velocity contrast area imaging, such as sweet spot (Tang et al., 2009) and gas chimney zones identification (Caldwell, 1999; Granli et al., 1999; Liu, 2019; Zhao et al., 2018a). In ERTM, P-waves typically yield images with high illumination and energy, while P-to-S converted waves enhance imaging resolution owing to their short wavelengths. The application of P/S wave-mode decomposition leads to marked improvements in ERTM images (Zhou et al., 2022; Zhang et al., 2022b).

For P/S wave-mode decomposition in isotropic media, Helmholtz decomposition (Morse and Feshbach, 1953; Dellinger and Etgen, 1990; Sun et al., 2001) is commonly used for generating scalar P and vector S waves. To ensure the vectorial equivalence to the original wavefield, Zhu (2017) developed a vector decomposing approach via building Poisson equation. Furthermore, this method is improved by Zhao et al. (2018b) and Yang et al. (2018) via time integration in wavelet and seismic records. While in anisotropic media, Helmholtz decomposition fails to properly decouple P/S wave-modes due to the misalignment between elastic wave propagation and polarization directions (Tsvankin, 2012). Dellinger and Etgen (1990) calculated a VTI P-wave

* Corresponding author.
E-mail address: cup_lele@163.com (L.-L. Zhang).
Peer review under the responsibility of China University of Petroleum (Beijing).

https://doi.org/10.1016/j.petsci.2026.01.036
1995-8226/

decomposing operator from Christoffel equation, delineating a principled framework for elastic wave decomposition in anisotropic media. Subsequently, Zhang and McMechan (2010) derived a wavenumber domain P/S wave decoupling formula via solving Christoffel equation. To adapt to heterogeneous media, many useful mathematical tools (Yan and Sava, 2009; Cheng and Fomel, 2014; Yu et al., 2016; Wang et al., 2018; Yang et al., 2019; Zhang et al., 2022a, 2023b; Zheng and Yao, 2023; Fang et al., 2024; Liu et al., 2024) are proposed to help decouple P/S waves in complex anisotropic models. Moreover, in order to improve efficiency, a Poynting-based Helmholtz decomposition algorithm are developed to solve the anisotropic vector P/S waves (Tang et al., 2009; Lu et al., 2019; Zhang et al., 2023a; Yao et al., 2024; Fan et al., 2024; Fang et al., 2025). They start to fastly calculate approximate P-wavefield and utilize it to obtain accurate propagating angles. These angles are finally used to calculate correct P/S waves. This method is efficient but easily disrupted by complex waveforms.

In addition to anisotropic P/S wave-mode decomposition, ERTM is also contaminated with low-frequency noise and false images. The former term results from identical wave propagation paths in both source and receiver wavefields, while the latter arises from encountering strong velocity contrasts within the migration model (Fei et al., 2014). To suppress these artifacts, geophysicists propose many effective methods such as non-reflection wave equation (Baysal et al., 1984), Laplace filtering (Zhang and Sun, 2009) and up/down going wavefield separation (Liu et al., 2011; Shen and Albertin, 2015; Zhang et al., 2021). Compared to other methods, up/down going wave separation demonstrates superior performance in suppressing false interface and low-frequency contamination in RTM results, without compromising the original seismic bandwidth. Liu et al. (2011) developed an implicit up/down wavefield separation, serving as RTM imaging condition. Fei et al., 2015 presented deprimary imaging method, suggesting only correlating down-going source wavefield with up-going receiver wavefield. To obtain explicit up/down going waves, Shen and Albertin (2015) used Hilbert transformed wavelet for additional once wavefield extrapolation with acoustic equation. Wang et al. (2016) extended explicitly up/down separation to isotropic elastic media. However, the twice wavefield extrapolation require much computation and memory especially in 3D space. To improve the efficiency, Revelo and Pestana (2019) proposed single propagation-based up/down wavefield separation approach for acoustic RTM imaging. They utilize acoustic dispersion relationship to calculate Hilbert transformed wavefields in temporal direction instead of solving the wave equation again. However, efficient explicit up/down separation in anisotropic-elastic media remains an open challenge and requires further investigation.

In this paper, we extend Zhang et al. (2023a)'s method to pure space domain via eliminating the phase-angle compensated term, which compute vector P/S wavefields with approximated amplitude and correct travel time. Then, we propose an efficient VTI elastic up/down going wave separating operator. We also embed this separating operator into P/S wave-mode decomposition formulation. A highly efficient up/down P/S wave-mode decomposition approach is developed and successfully applied in VTI ERTM.

The structure of our paper is shown as follows: We first introduce P/S wave-mode decomposition approach. Then a VTI elastic up/down going separated operator is presented and embed into P/S decoupling formula. Simple and complex models are finally used to test our proposed method.

2. Efficient P/S wave-mode decomposition approach in VTI media

Decoupling P/S waves during propagation requires determining their polarized directions. In VTI media, the P/S wave polarization vector and dispersion formulation can be calculated from Christoffel equation and expressed as (Tsvankin, 2012; Zhang et al., 2022a)

$$\mathbf{D}^{\mathrm{P}} = \begin{bmatrix} k_x \\ \dfrac{\sqrt{\left[(1+2\delta)v_{\mathrm{p}}^2 - v_{\mathrm{s}}^2\right]\left[v_{\mathrm{p}}^2 - v_{\mathrm{s}}^2\right]}}{(1+2\epsilon)v_{\mathrm{p}}^2 - v_{\mathrm{s}}^2} k_z \end{bmatrix}, \quad \mathbf{D}^{\mathrm{S}} = \begin{bmatrix} \dfrac{\sqrt{\left[(1+2\delta)v_{\mathrm{p}}^2 - v_{\mathrm{s}}^2\right]\left[v_{\mathrm{p}}^2 - v_{\mathrm{s}}^2\right]}}{(1+2\epsilon)v_{\mathrm{p}}^2 - v_{\mathrm{s}}^2} k_z \\ -k_x \end{bmatrix}, \tag{1}$$

and

$$\begin{aligned} \rho\omega^2 &= \rho v_{\mathrm{p}}^2\left[(1+2\epsilon)k_x^2 + k_z^2\right], \\ \rho\omega^2 &= \rho v_{\mathrm{s}}^2\left[k_x^2 + k_z^2\right], \end{aligned} \tag{2}$$

The detailed derivation of Eqs. (1) and (2) can be found in Zhang et al. (2022a). $\mathbf{D}^{\mathrm{P}}$ and $\mathbf{D}^{\mathrm{S}}$ of Eq. (1) are the P- and S-waves polarization vectors, respectively. As shown in Eq. (2), it represents the dispersion relationship of the P- and S-waves. k_x and k_z are x- and z-components of wavenumber, v_{p} and v_{s} are vertical P- and S-wave velocities, ϵ and δ are anisotropic parameters, ρ is the density, and ω is circular frequency.

Elastic vector wavefield $\mathbf{U}$ is built as summation of P- and S-waves, which is expressed as

$$\mathbf{U} = \mathbf{U}^{\mathrm{P}} + \mathbf{U}^{\mathrm{S}}, \tag{3}$$

where $\mathbf{U}^{\mathrm{P}}$ and $\mathbf{U}^{\mathrm{S}}$ are vector P- and S-wavefield in wavenumber domain. The projection of $\mathbf{U}$, $\mathbf{U}^{\mathrm{P}}$ and $\mathbf{U}^{\mathrm{S}}$ onto polarization vectors (Eq. (1)) gives

$$\begin{aligned} &\mathbf{D}^{\mathrm{P}}\cdot\mathbf{U} = \mathbf{D}^{\mathrm{P}}\cdot\mathbf{U}^{\mathrm{P}}, \\ &\mathbf{D}^{\mathrm{S}}\cdot\mathbf{U} = \mathbf{D}^{\mathrm{S}}\cdot\mathbf{U}^{\mathrm{S}}, \\ &\mathbf{D}^{\mathrm{S}}\cdot\mathbf{U}^{\mathrm{P}} = 0, \\ &\mathbf{D}^{\mathrm{P}}\cdot\mathbf{U}^{\mathrm{S}} = 0. \end{aligned} \tag{4}$$

The unknown variables of Eq. (4) are vectors $\mathbf{U}^{\mathrm{P}}$ and $\mathbf{U}^{\mathrm{S}}$ and their solutions are expressed as

$$\begin{aligned} \mathbf{U}^{\mathrm{P}} &= \mathbf{D}^{\mathrm{P}}\left(\mathbf{D}^{\mathrm{P}}\cdot\mathbf{U}^{\mathrm{P}}\right)\Big/|\mathbf{D}^{\mathrm{P}}|^2, \\ \mathbf{U}^{\mathrm{S}} &= \mathbf{D}^{\mathrm{S}}\left(\mathbf{D}^{\mathrm{S}}\cdot\mathbf{U}^{\mathrm{S}}\right)\Big/|\mathbf{D}^{\mathrm{S}}|^2, \end{aligned} \tag{5}$$

Eq. (5) is P/S wave decomposing formulation in the wavenumber domain. The difficulty of implementation for this formula is to deal with the denominators $|\mathbf{D}^{\mathrm{P}}|^2$ and $|\mathbf{D}^{\mathrm{S}}|^2$ (apparently $|\mathbf{D}^{\mathrm{P}}|^2 = |\mathbf{D}^{\mathrm{S}}|^2 = k_x^2 + r^2 k_z^2$). Noting that these denominators mainly influence the amplitudes and frequency band of decomposed P/S wavefields, we rewrite Eq. (5) as

$$\mathbf{U}^{\mathrm{P}} = \frac{\mathbf{D}^{\mathrm{P}}\left(\mathbf{D}^{\mathrm{P}}\cdot\mathbf{U}\right)}{\left|\mathbf{K}_1\right|^2}\cdot\frac{\left|\mathbf{K}_1\right|^2}{\left|\mathbf{D}^{\mathrm{P}}\right|^2}, \quad \mathbf{U}^{\mathrm{S}} = \frac{\mathbf{D}^{\mathrm{S}}\left(\mathbf{D}^{\mathrm{S}}\cdot\mathbf{U}\right)}{\left|\mathbf{K}_2\right|^2}\cdot\frac{\left|\mathbf{K}_2\right|^2}{\left|\mathbf{D}^{\mathrm{S}}\right|^2}, \tag{6}$$

with

$$\left|\mathbf{K}_1\right|^2 = \omega^2 = v_{\mathrm{p}}^2\left[(1+2\epsilon)k_x^2 + k_z^2\right], \quad \left|\mathbf{K}_2\right|^2 = \omega^2 = v_{\mathrm{s}}^2\left[k_x^2 + k_z^2\right]. \tag{7}$$

It is worthy noting that the wavenumber components k_x and k_z are canceled out in $\frac{|\mathbf{K}_1|^2}{|\mathbf{D}^{\mathrm{P}}|^2}$ and $\frac{|\mathbf{K}_2|^2}{|\mathbf{D}^{\mathrm{S}}|^2}$ due to $k_x^2/k_z^2 = \tan^2\theta$ (θ is the phase velocity angle) (Zhang et al., 2023a). Therefore, $\frac{|\mathbf{K}_1|^2}{|\mathbf{D}^{\mathrm{P}}|^2}$ and $\frac{|\mathbf{K}_2|^2}{|\mathbf{D}^{\mathrm{S}}|^2}$ solely affect the amplitudes of the decomposed P-waves and S-waves, keeping their phases or travel time. This means we can remove those two terms in Eq. (6) and shall not impact on the ERTM image in anisotropic media.

After eliminating $\frac{|\mathbf{K}_1|^2}{|\mathbf{D}^{\mathrm{P}}|^2}$ and $\frac{|\mathbf{K}_2|^2}{|\mathbf{D}^{\mathrm{S}}|^2}$ in Eq. (6), we convert it to space domain as

$$\mathbf{u}^{\mathrm{p}}(\mathbf{x},\mathbf{t}) = \nabla^{\mathrm{p}}(\nabla^{\mathrm{p}}\cdot\mathbf{u}''(\mathbf{x},\mathbf{t})), \quad \mathbf{u}^{\mathrm{s}}(\mathbf{x},\mathbf{t}) = \nabla^{\mathrm{s}}(\nabla^{\mathrm{s}}\cdot\mathbf{u}''(\mathbf{x},\mathbf{t})), \tag{8}$$

where $\mathbf{u}^{\mathrm{p}}$ and $\mathbf{u}^{\mathrm{s}}$ are vector P- and S-wavefield in the space domain, $\mathbf{u}''$ is the inverse Fourier transform of $\mathbf{U}/\omega^2$, $\mathbf{x} = (x, z)$ is two-dimensional Cartesian coordinate, t is time. To avoid storing full wavefields and performing FFT (fast Fourier transform)-based computations, $\mathbf{u}''$ can be efficiently derived by temporally extrapolating the elastic wavefield using a twice-integrated wavelet (or seismic records in recever side). $\nabla^{\mathrm{p}} = [\partial_x \quad r\partial_z]^{\mathrm{T}}$ and $\nabla^{\mathrm{s}} = [r\partial_z \quad -\partial_x]^{\mathrm{T}}$ are P/S wave decomposing operators in space domain, ∂_x and ∂_z are 1-order partial derivative in x- and z-axis direction. $r = \frac{\sqrt{\left[(1+2\delta)v_{\mathrm{p}}^2 - v_{\mathrm{s}}^2\right]\left[v_{\mathrm{p}}^2 - v_{\mathrm{s}}^2\right]}}{(1+2\epsilon)v_{\mathrm{p}}^2 - v_{\mathrm{s}}^2}$ is the model coefficient. The decomposed P/S wavefields produced by Eq. (8), with correct travel times, phases, and approximated amplitudes, are obtained through only a few partial differential calculations, providing sufficient accuracy for ERTM imaging.

3. Up/down wavefield separation approach in elastic VTI media

Conventional cross-correlation image condition usually generates low-frequency noise and false images. To solve this problem, up/down wavefield separation imaging condition is proposed in RTM as

$$I(\mathbf{x}) = \int_0^T S_{\mathrm{d}}(\mathbf{x},t)R_{\mathrm{u}}(\mathbf{x},t)\mathrm{d}t, \tag{9}$$

where $I(\mathbf{x})$ is RTM image, $S_{\mathrm{d}}(\mathbf{x}, t)$ is the down-doing wavefield and $R_{\mathrm{u}}(\mathbf{x}, t)$ is the up-going receiver wavefield. Eq. (9) mitigates common artifacts in conventional reverse-time migration (RTM) by not only avoiding the correlation of source and receiver wavefields along identical propagation paths but also suppressing spurious imaging effects through the targeted correlation of up-going source waves with down-going receiver waves at strong gradient interfaces.

To explicitly obtain the up/down wavefield, Shen and Albertin (2015) developed a separating formulation as

$$S^{\mathrm{d}}(\mathbf{x},t) = \frac{1}{2}(1 + H_z H_t)S(\mathbf{x},t), \quad R^{\mathrm{u}}(\mathbf{x},t) = \frac{1}{2}(1 - H_z H_t)R(\mathbf{x},t), \tag{10}$$

where H_z and H_t are the Hilbert transform along z-axis and temporal direction. For the implementation of operator H_t, it requires to perform Hilbert transform on source wavelet and then extrapolate additional source wavefield. The same way also needs in receiver wavefields. This is effective but requires substantial computation and memory especial in elastic media. An alternative method for acoustic media is to calculate the Hilbert transformed wavefield during the propagation (Zhang and Zhang, 2009; Revelo and Pestana, 2019). In this paper, we aim to extend it to elastic VTI media.

To start with, the operator $H_z H_t$ can be defined in wavenumber-frequency domain as

$$H_z H_t = \frac{ik_z}{|k_z|}\frac{i\omega}{|\omega|}, \tag{11}$$

where $i = \sqrt{-1}$. In terms of Eq. (2), we replace ω of Eq. (11) with wavenumber and model parameters as

$$(H_z H_t)^{\mathrm{P}} = \frac{ik_z}{|k_z|}\frac{i\omega}{v_{\mathrm{p}}\sqrt{\left[(1+2\epsilon)k_x^2 + k_z^2\right]}}, \tag{12a}$$

$$(H_z H_t)^{\mathrm{S}} = \frac{ik_z}{|k_z|}\frac{i\omega}{v_{\mathrm{s}}\sqrt{\left[k_x^2 + k_z^2\right]}}, \tag{12b}$$

where $(H_z H_t)^{\mathrm{P}}$ and $(H_z H_t)^{\mathrm{S}}$ are Hilbert transform operators for P- and S-wave, respectively. Note that model parameter ϵ exists in denominator of Eq. (12a), limiting this formula to homogeneous media. According to weakly anisotropic assumption (Thomsen, 1986), we perform first-order Taylor expansion on Eq. (12a) around $\epsilon = 0$ and then convert Eq. (12) into space-wavenumber domain as

$$(H_z H_t)^{\mathrm{P}} = \frac{1}{v_{\mathrm{p}}}\left[\frac{1}{|k_z|\left(k_x^2 + k_z^2\right)^{1/2}} - \frac{k_x^2\epsilon}{|k_z|\left(k_x^2 + k_z^2\right)^{3/2}}\right]\frac{\partial}{\partial z}\frac{\partial}{\partial t}, \tag{13a}$$

$$(H_z H_t)^{\mathrm{S}} = \frac{1}{v_{\mathrm{s}}}\left[\frac{1}{|k_z|\left(k_x^2 + k_z^2\right)^{1/2}}\right]\frac{\partial}{\partial z}\frac{\partial}{\partial t}, \tag{13b}$$

where ∂_z and ∂_t is 1-order derivative along z-axis and temporal direction. Using Eq. (13), the Hilbert transformed wavefield required in Eq. (10) can be calculated during single propagation, instead of additionally solving wave equation. The detailed workflow of Eqs. (10) and (13) is shown in Algorithm 1. As observed, only once forward and two inverse FFTs are required for P- (Eq. (13a)) and S-wavefield (Eq. (13b)) separation, respectively.

Algorithm 1
Up/down wavefield separation for P/S waves in VTI media.

Input: anisotropic scalar P-wavefield $u^{\mathrm{p}}(z, t)$ and S-wavefield $u^{\mathrm{s}}(z, t)$
Output: up/down going P- and S-wavefields $u^{\mathrm{p}}_{\mathrm{u}}(z,t)$, $u^{\mathrm{p}}_{\mathrm{d}}(z,t)$, $u^{\mathrm{s}}_{\mathrm{u}}(z,t)$ and $u^{\mathrm{s}}_{\mathrm{d}}(z,t)$
for t time step do
1. $(u^{\mathrm{p}})'' \leftarrow \dfrac{\partial^2 u^{\mathrm{p}}}{\partial z \partial t}$, $\quad (u^{\mathrm{s}})'' \leftarrow \dfrac{\partial^2 u^{\mathrm{s}}}{\partial z \partial t}$,
2. $U^{\mathrm{P}} \leftarrow \mathrm{FFT}[(u^{\mathrm{p}})'']$, $\quad U^{\mathrm{S}} \leftarrow \mathrm{FFT}[(u^{\mathrm{s}})'']$,
3. $u^{\mathrm{p}}_{\mathrm{a}} \leftarrow \mathrm{FFT}^{-1}\left[U^{\mathrm{P}} \cdot \dfrac{1}{|k_z|\left(k_x^2+k_z^2\right)^{1/2}}\right]$, $\quad u^{\mathrm{p}}_{\mathrm{b}} \leftarrow \mathrm{FFT}^{-1}\left[U^{\mathrm{P}} \cdot \dfrac{k_x^2}{|k_z|\left(k_x^2+k_z^2\right)^{3/2}}\right]\epsilon$, $u^{\mathrm{s}}_{\mathrm{a}} \leftarrow \mathrm{FFT}^{-1}\left[U^{\mathrm{S}} \cdot \dfrac{1}{|k_z|\left(k_x^2+k_z^2\right)^{1/2}}\right]$,
4. $u^{\mathrm{p}}_{\mathrm{H}} \leftarrow \dfrac{1}{v_{\mathrm{p}}}\left(u^{\mathrm{p}}_{\mathrm{a}} - u^{\mathrm{p}}_{\mathrm{b}} \cdot \epsilon\right)$, $\quad u^{\mathrm{s}}_{\mathrm{H}} \leftarrow \dfrac{1}{v_{\mathrm{s}}} u^{\mathrm{s}}_{\mathrm{a}}$,
5. $u^{\mathrm{p}}_{\mathrm{u}} = \dfrac{1}{2}(u^{\mathrm{p}} - u^{\mathrm{p}}_{\mathrm{H}})$, $\quad u^{\mathrm{p}}_{\mathrm{d}} = \dfrac{1}{2}(u^{\mathrm{p}} + u^{\mathrm{p}}_{\mathrm{H}})$, $u^{\mathrm{s}}_{\mathrm{u}} = \dfrac{1}{2}(u^{\mathrm{s}} - u^{\mathrm{s}}_{\mathrm{H}})$, $\quad u^{\mathrm{s}}_{\mathrm{d}} = \dfrac{1}{2}(u^{\mathrm{s}} + u^{\mathrm{s}}_{\mathrm{H}})$,

end for
where FFT and FFT^{-1} are 2D forward and inverse FFT performed to the anisotropic wavefields. For simplicity, the coordinates of wavefields are omitted in steps 1 to 5.

In last subsection, we propose a vector P/S wave-mode decomposition method that produces four wave components u_x^{p}, u_z^{p}, u_x^{s} and u_z^{s} (Eq. (8)). Performing Algorithm 1 on each of those waves will generate much computation. To improve the efficiency, we embed Eq. (10) into Eq. (8) as

$$\begin{aligned} \mathbf{u}^{\mathrm{P}}(\mathbf{x},t)_{\mathrm{u/d}} &= \frac{1}{2}\nabla^{\mathrm{P}}(1 \pm H_z H_t)(\nabla^{\mathrm{P}} \cdot \mathbf{u}''(\mathbf{x},t)), \\ \mathbf{u}^{\mathrm{S}}(\mathbf{x},t)_{\mathrm{u/d}} &= \frac{1}{2}\nabla^{\mathrm{S}}(1 \pm H_z H_t)(\nabla^{\mathrm{S}} \cdot \mathbf{u}''(\mathbf{x},t)), \end{aligned} \tag{14}$$

where $\mathbf{u}^{\mathrm{p}}(\mathbf{x},t)_{\mathrm{u/d}}$ and $\mathbf{u}^{\mathrm{s}}(\mathbf{x},t)_{\mathrm{u/d}}$ denote up/down going vector P- and S-wavefields, respectively. Up- or down-going mode depends on sign of $\pm$ ("+" determines up-going wave and "−" produces down-going wave). Because of scalar $\nabla^{\mathrm{P}} \cdot \mathbf{u}''$ and $\nabla^{\mathrm{S}} \cdot \mathbf{u}''$, only one time implementation of Algorithm 1 is required for each term of Eq. (14), which efficiently achieve anisotropic P/S wave-mode decomposition and up/down going separation. The specific calculation procedure of Eq. (14) is shown in Algorithm 2.

and solve it with staggered grid finite difference and convolution perfectly match layer boundary condition.

4.1. Layered model

As first example, a VTI layered model (Fig. 1) is used for P/S wave-mode decomposition and up/down going separation test. The model size of 10,000 m × 2000 m is with a uniform spacing of 10 m. A 20 Hz Ricker wavelet, serving as an explosive source, is applied with a time interval of 1 ms. A single shot is positioned at (5000, 1800) m to generate elastic wavefields in both the x- and z-components (Fig. 2). In terms of Eq. (8), the original elastic VTI wavefields are decomposed into P-wave (Fig. 3(a) and (b)) and S-wave (Fig. 3(c) and (d)) components. For further analysis, a trace data selected from Figs. 2 and 3 at xline (distance axis) of 4000 m to facilitate comparison (Fig. 4). The red line denotes the simulated elastic wavefield, while the blue line corresponds to the decomposed P- and S-wave components. As demonstrated, the decomposed P/S-wave components exhibit accurate travel times and approximated amplitudes relative to the simulated elastic wavefields. Then, using Eq. (14), the decomposed P- and S-wavefields are separated into down-going (Fig. 5) as well as up-going P/S wave components (Fig. 6). To reduce the influence of zero-wavenumber components, we add a cosine triangle function window in both edges of data. Although this damages a little useful signal, the separated up/down P/S wavefields still keep correct travel time and phases as those of P/S wavefields, which are sufficient for ERTM.

Algorithm 2
Up/down and P/S wavefield decomposition for P/S waves in VTI media.

Input: anisotropic vector elastic wavefield $\mathbf{u}''(\mathbf{x}, t)$,
Output: up/down going vector P- and S-wavefields $\mathbf{u}^{\mathrm{p}}_{\mathrm{u}}(\mathbf{x},t)$, $\mathbf{u}^{\mathrm{p}}_{\mathrm{d}}(\mathbf{x},t)$, $\mathbf{u}^{\mathrm{s}}_{\mathrm{u}}(\mathbf{x},t)$ and $\mathbf{u}^{\mathrm{s}}_{\mathrm{d}}(\mathbf{x},t)$
for t time step do
1. $(u^{\mathrm{p}}) \leftarrow \nabla^{\mathrm{P}} \cdot \mathbf{u}''$, $(u^{\mathrm{s}}) \leftarrow \nabla^{\mathrm{S}} \cdot \mathbf{u}''$,
2. $u^{\mathrm{p}}_{\mathrm{u}} = (1 - H_z H_t)u^{\mathrm{p}}$, $\quad u^{\mathrm{p}}_{\mathrm{d}} = (1 + H_z H_t)u^{\mathrm{p}}$, $u^{s}_{u} = (1 - H_z H_t)u^{\mathrm{s}}$, $\quad u^{\mathrm{s}}_{\mathrm{d}} = (1 + H_z H_t)u^{\mathrm{s}}$,
3. $\mathbf{u}^{\mathrm{p}}_{\mathrm{u}} = \nabla u^{p}_{u}$, $\quad \mathbf{u}^{\mathrm{p}}_{\mathrm{d}} = \nabla u^{p}_{d}$, $\mathbf{u}^{\mathrm{s}}_{\mathrm{u}} = \nabla u^{s}_{u}$, $\quad \mathbf{u}^{\mathrm{s}}_{\mathrm{d}} = \nabla u^{s}_{d}$,

end for
where the calculation of $H_z H_t$ can refer to algorithm 1. For simplicity, the coordinates of wavefields are omitted in steps 1 to 3.

By using Eq. (14), a dot product correlation imaging condition is applied for VTI ERTM as

$$\begin{aligned} I^{\mathrm{PP}}(\mathbf{x}) &= \int_0^T \mathbf{S}^{\mathrm{P}}_{\mathrm{d}}(\mathbf{x},t)\mathbf{R}^{\mathrm{P}}_{\mathrm{u}}(\mathbf{x},t)\mathrm{d}t, \\ I^{\mathrm{PS}}(\mathbf{x}) &= \int_0^T \mathbf{S}^{\mathrm{P}}_{\mathrm{d}}(\mathbf{x},t)\mathbf{R}^{\mathrm{S}}_{\mathrm{u}}(\mathbf{x},t)\mathrm{d}t, \end{aligned} \tag{15}$$

where $I^{\mathrm{PP}}(\mathbf{x})$ and $I^{\mathrm{PS}}(\mathbf{x})$ are PP- and PS-images, $\mathbf{S}^{\mathrm{P}}_{\mathrm{d}}(\mathbf{x},t)$ are vectors down-going P-wavefield in source side, $\mathbf{R}^{\mathrm{P}}_{\mathrm{u}}(\mathbf{x},t)$ and $\mathbf{R}^{\mathrm{P}}_{\mathrm{d}}(\mathbf{x},t)$ are vector up- and down-going S-wavefields in receiver side.

4. Example

In this section, we present two examples via VTI layered and Hess models. We apply first-order stress-velocity wave equation

4.2. VTI Hess model

The second numerical experiment is conducted on the VTI Hess model, constructed with a grid dimension of 1200 × 500 and a uniform spacing of 10 m (Fig. 7). The S-wave velocity field is derived by scaling the P-wave velocity by a factor of 2.0. A 15 Hz Ricker wavelet is employed as the explosive source. The time

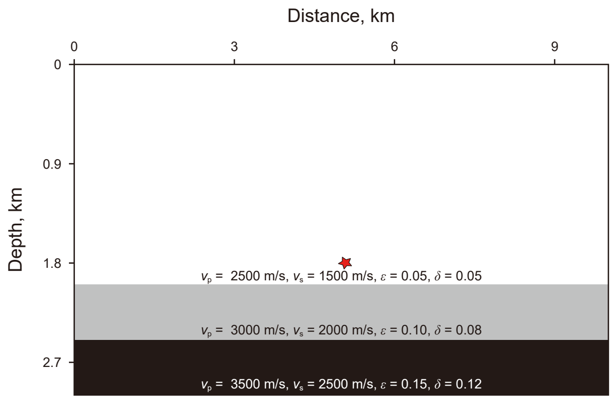

Fig. 1. Model parameters for the VTI layered model. The star denotes the source located at (5000 m, 1800 m).

sampling interval of 1 ms. A single seismic source is positioned at coordinates (6000 m, 2000 m) to excite elastic wave. Fig. 8 displays the original vector wavefields, comprising both *x*- and *z*-components. Then our developed decomposing method (Eq. (8)) successfully isolates the theses coupled wavefields into P- and S-wave modes, as demonstrated in Fig. 9. Similar to those of decomposed P/S wavefields in Fig. 3, these wave components possess correct travel time and approximate amplitudes. Moreover, the up/down wavefield separating operator (Eq. (14)) is applied to those P/S wavefields and generate up- and down-going wave components (Figs. 10 and 11), which are used for imaging in VTI ERTM.

For VTI ERTM imaging experiment, a total of 600 shots were placed with uniform spacing of 20 m at a constant depth of 100 m. Each shot was recorded by an array of 300 receivers to capture the seismic signal. During the wavefield propagation process, the elastic wavefields were dynamically separated into up-going and

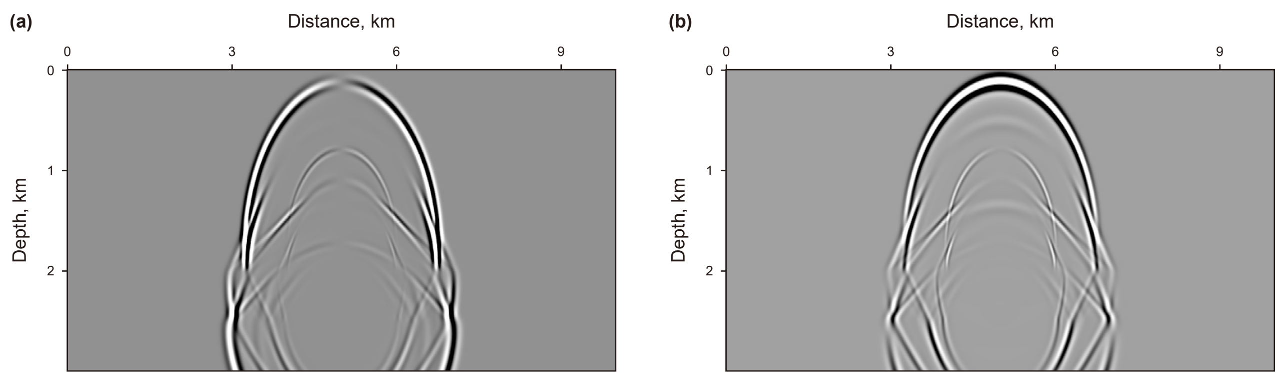

Fig. 2. The **(a)** *x*- and **(b)** *z*-components of elastic displacement wavefields for the layered model at propagating time 0.8 s.

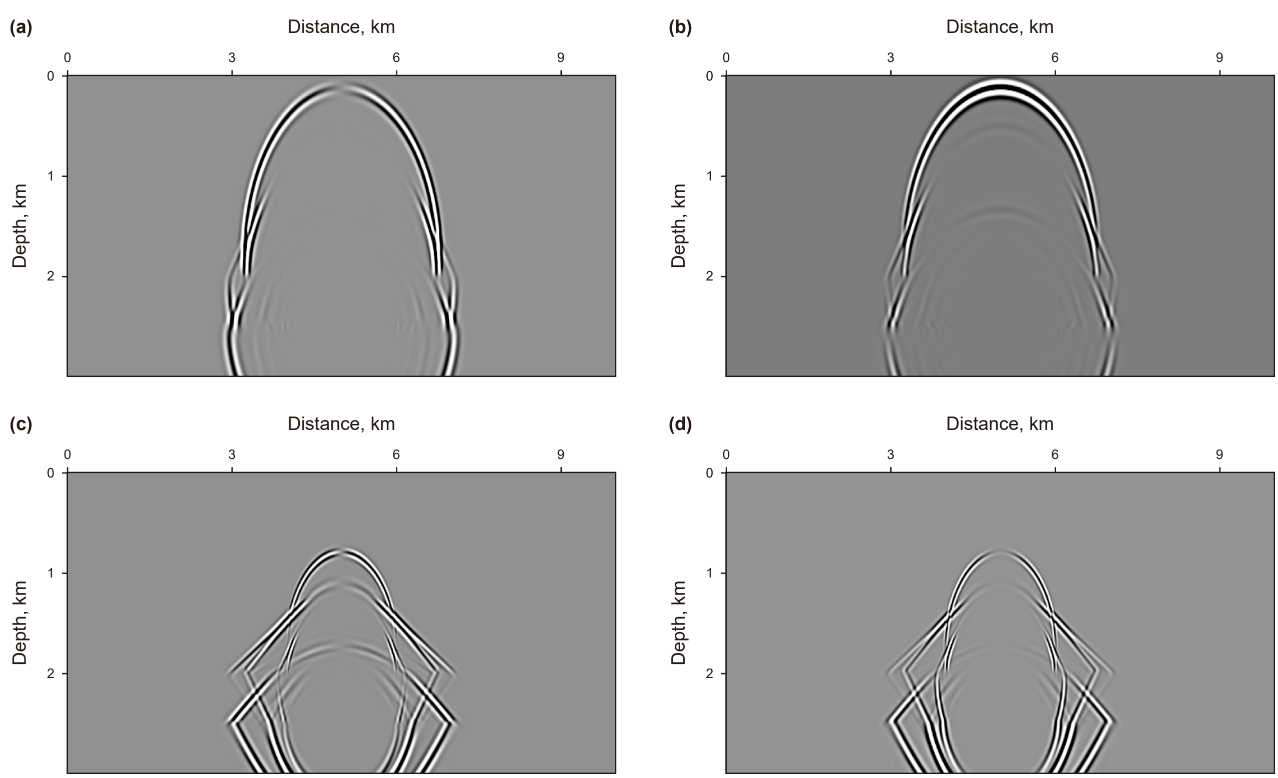

Fig. 3. The decomposed P-wave **(a)** *x*- and **(b)** *z*-components, and S-wave **(c)** *x*- and **(d)** *z*-components for the layered model at propagating time 0.8 s.

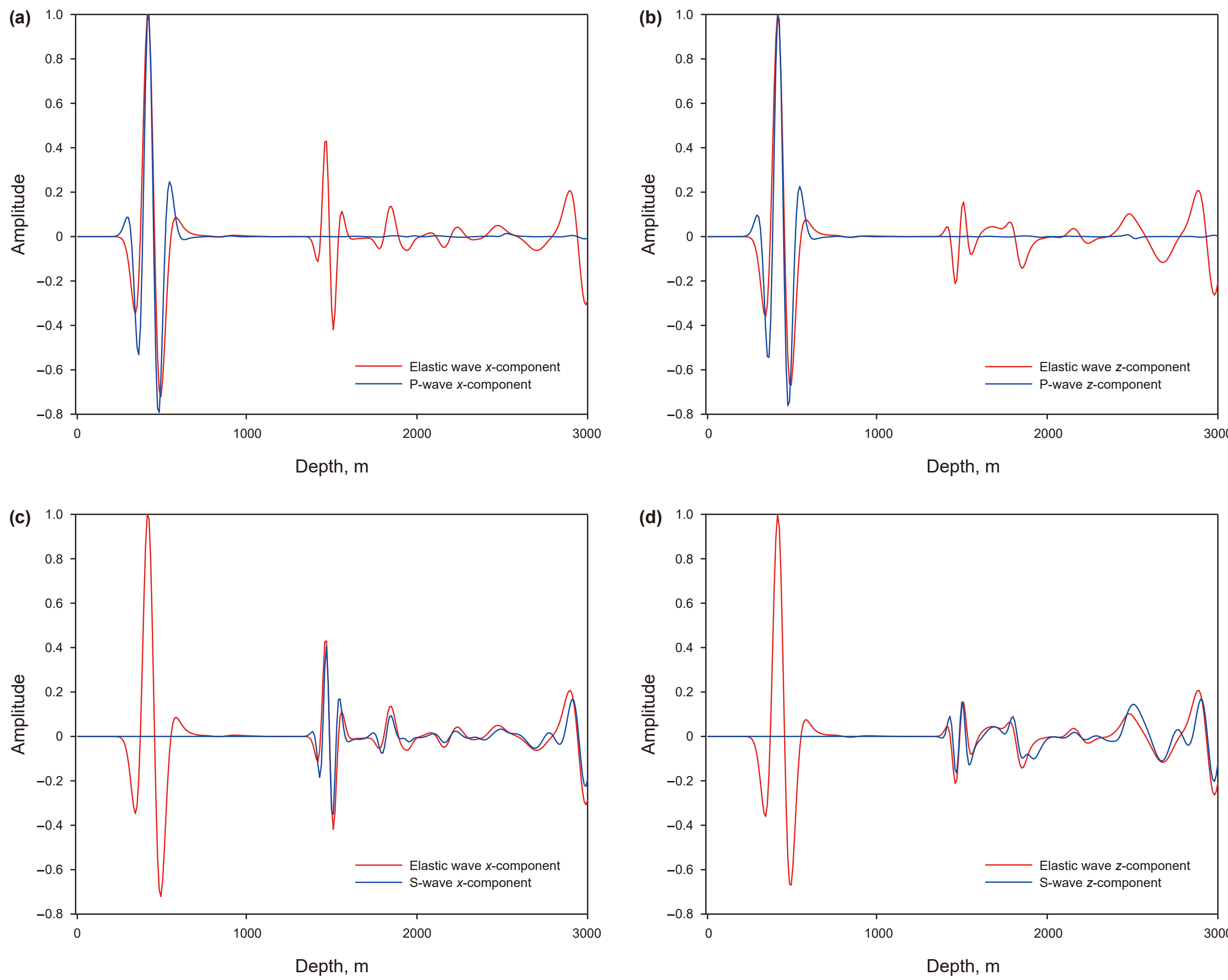

Fig. 4. Comparison of single trace data extracted from elastic wavefield and P/S wavefield (Figs. 2 and 3) at distance = 4000 m. Panel **(a)** and (**b**) are x- and z-components of elastic and P-wavefields, **(c)** and **(d)** denotes x- and z-components of elastic and S-wavefields. The red lines are elastic wavefield data and blue lines indicate P/S wave data.

down-going P- and S-wave components at each time step. Fig. 12(a) present conventional PP-image contaminated with severe low-frequency noise (indicated by red arrows). While Fig. 12(c) denotes PP-image via up/down separation imaging condition (Eq. (15)) with clear imaging effect. Fig. 12(b) is conventional PS-image that exist apparent false images in the strong velocity contrast (indicated by red arrows). Through up/down separation imaging condition, those artifacts are suppressed in PS-image of Fig. 12(d) which improves the image quality. Note that artifacts (indicated by circles) caused by multiple and converted wave also exist in Fig. 12(c) and (d), which can be removed from multiple waves imaging.

5. Discussion

We present an efficient P/S and up/down wavefield separation approach in elastic VTI media with single propagation. Our method adapts to arbitrary complex models and afford low-cost computation. It effectively suppresses the common artifacts existed in conventional ERTM and improve the imaging quality. However, our proposed method is derived based on some assumptions and approximations, which has to pay attention for some deficiency. First of all, the polarization vector is derived based on elliptical assumption. Implementation in strongly non-elliptical media may reveal intrinsic error characteristics in our method. The applying effect analysis of our approach under elliptical assumption can be found in Zhang et al. (2022a). Meantime, in the P/S wave-mode decomposition formula (Eq. (8)), the amplitude terms $\frac{|\mathbf{K}_1|^2}{|\mathbf{D}^{\mathrm{P}}|^2}$ and $\frac{|\mathbf{K}_2|^2}{|\mathbf{D}^{\mathrm{S}}|^2}$ are eliminated. Although this way shall not influence on ERTM imaging, the angle domain or offset domain common image gathers produced from ERTM may not be in accord with AVO (amplitude versus offset) response.

First-order Taylor expansion is used for deriving Hilbert transform operator of P-wave. This is implemented based on weakly anisotropic media assumption. When ϵ is far greater than zero, our up/down wave separation method may give an unclear separating result for P-wavefield. To present the computational accuracy of derived Hilbert transformation formula, a

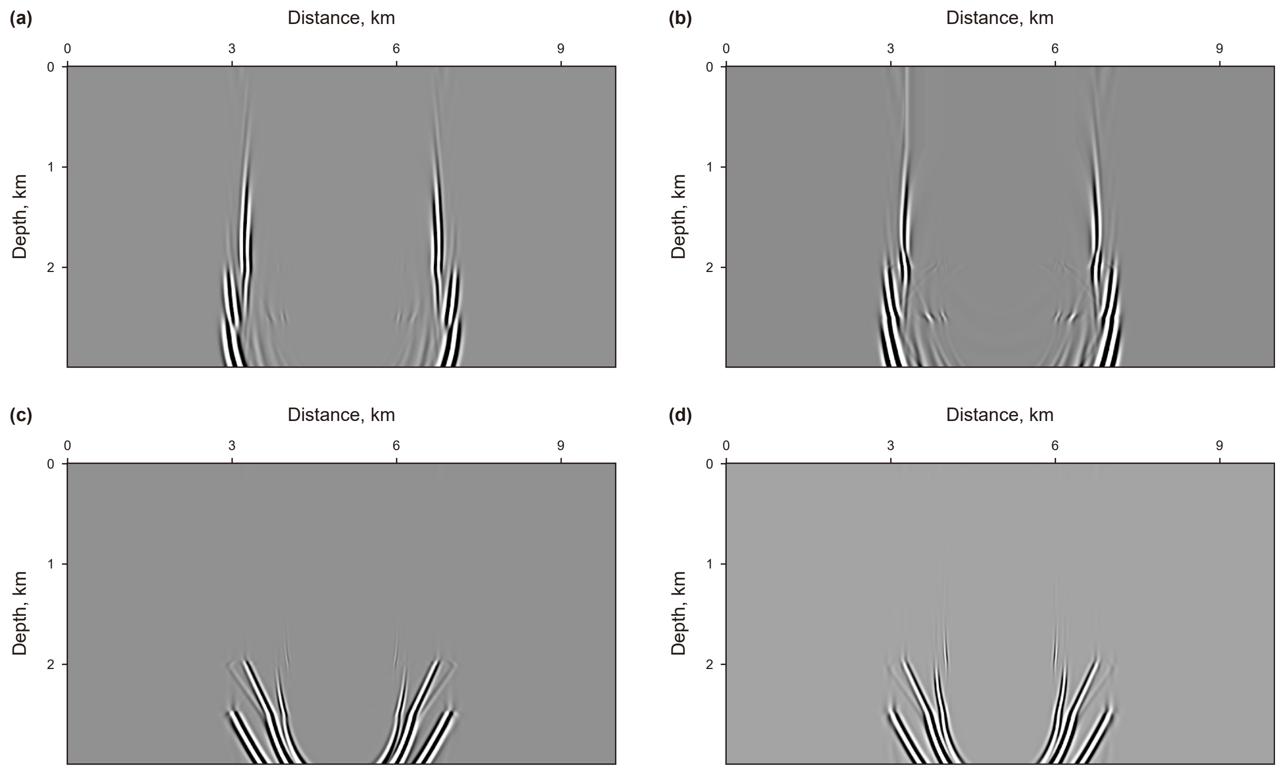

Fig. 5. The separated down-going P-wave **(a)** *x*- and **(b)** *z*-components, and down-going S-wave **(c)** *x*- and **(d)** *z*-components for the layered model at propagating time 0.8 s.

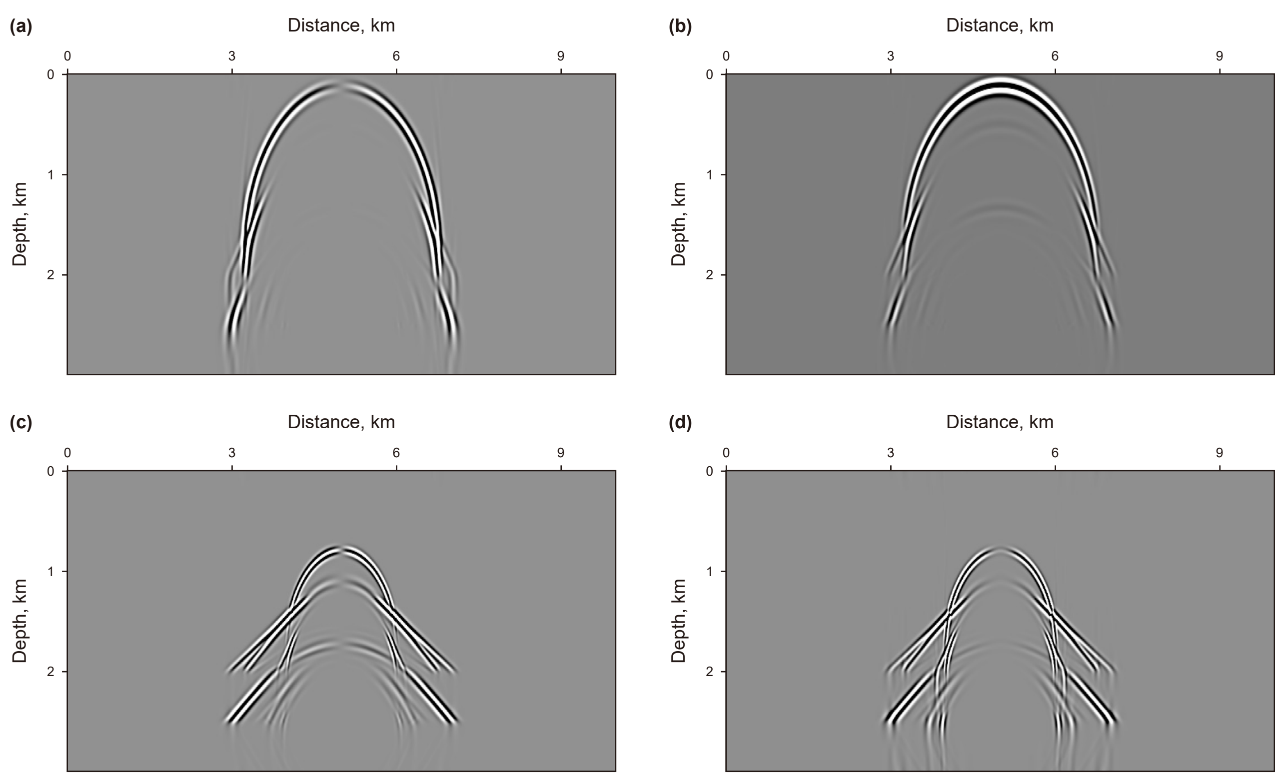

Fig. 6. The separated up-going P-wave **(a)** *x*- and **(b)** *z*-components, and up-going S-wave **(c)** *x*- and **(d)** *z*-components for the layered model at propagating time 0.8 s.

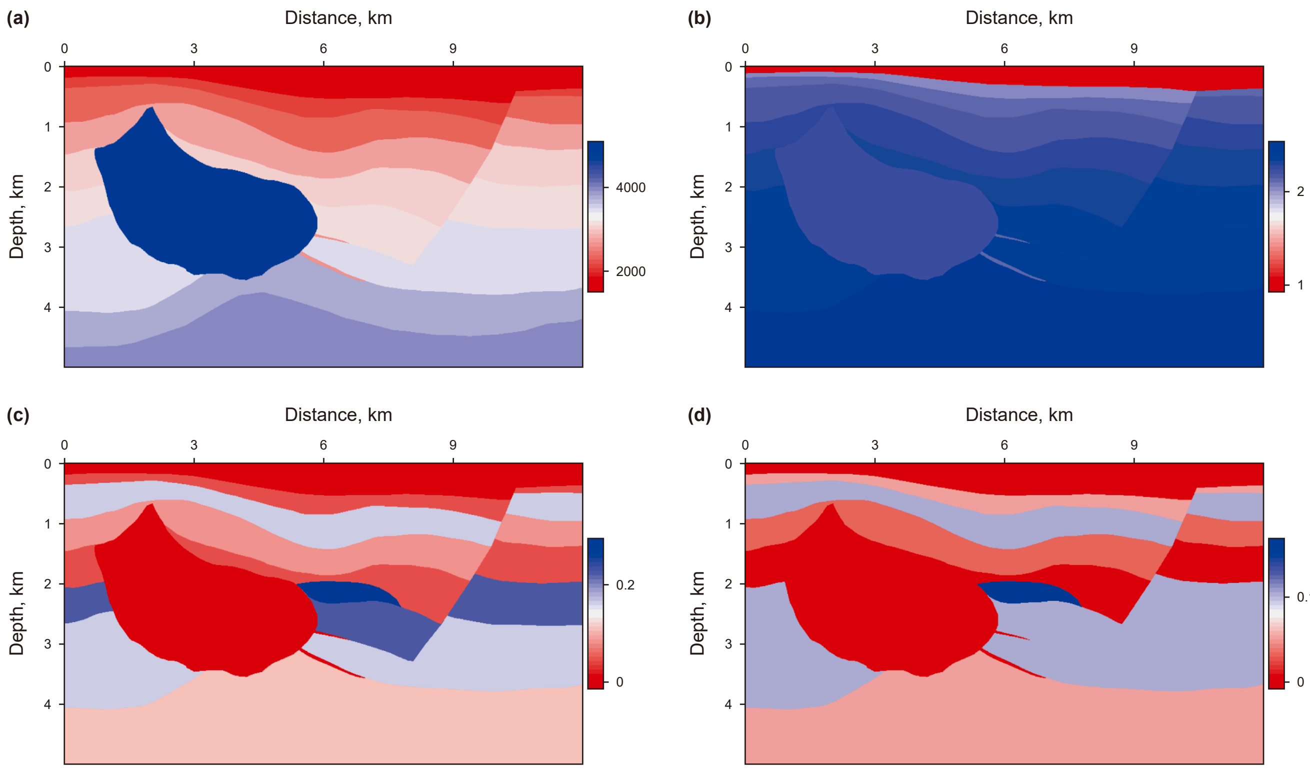

Fig. 7. The VTI Hess model parameters **(a)** v_p, **(b)** ρ, **(c)** ϵ and **(d)** δ.

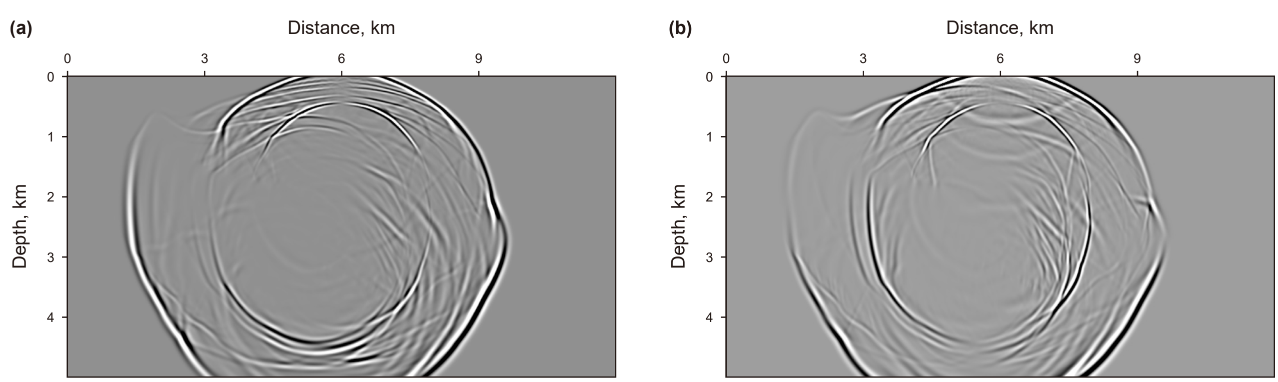

Fig. 8. The **(a)** x- and **(b)** z-components of elastic displacement wavefields for the VTI Hess model at propagating time 1.2 s.

homogeneous medium are used for test. The P-wave velocity is chosen as 2500 m/s and main frequency is 15 Hz. Three pairs of wavenumber components are applied with $k_x = k_z = 0.001$, $k_x = k_z = 0.025$ and $k_x = k_z = 0.05$. Fig. 13 presents amplitude of Hilbert transformation calculated from Eqs. (12a) and (13a). As observed, the difference between analytical (red line using Eq. (12a)) and approximate (blue line using Eq. (13a)) solution increase with *epsilon* varying from 0 to 0.5. However, the relative error is only 2.67% for each case (Fig. 13(a),(b) and (c)), which is accordance with the good ERTM image effect in VTI Hess model (whose maximum ε is about 0.4).

Our method can be easily extended to three-dimensional (3D) VTI media and TTI media. For 3D space, the S-wave includes SV- and SH-wave modes which have their own polarization vectors solved in Christoffel equation. They keep the similar decomposing formation to Eq. (8). For converting VTI media to TTI media, bond transform can be used with the rotating angle between z-axis and symmetric axis of TI media.

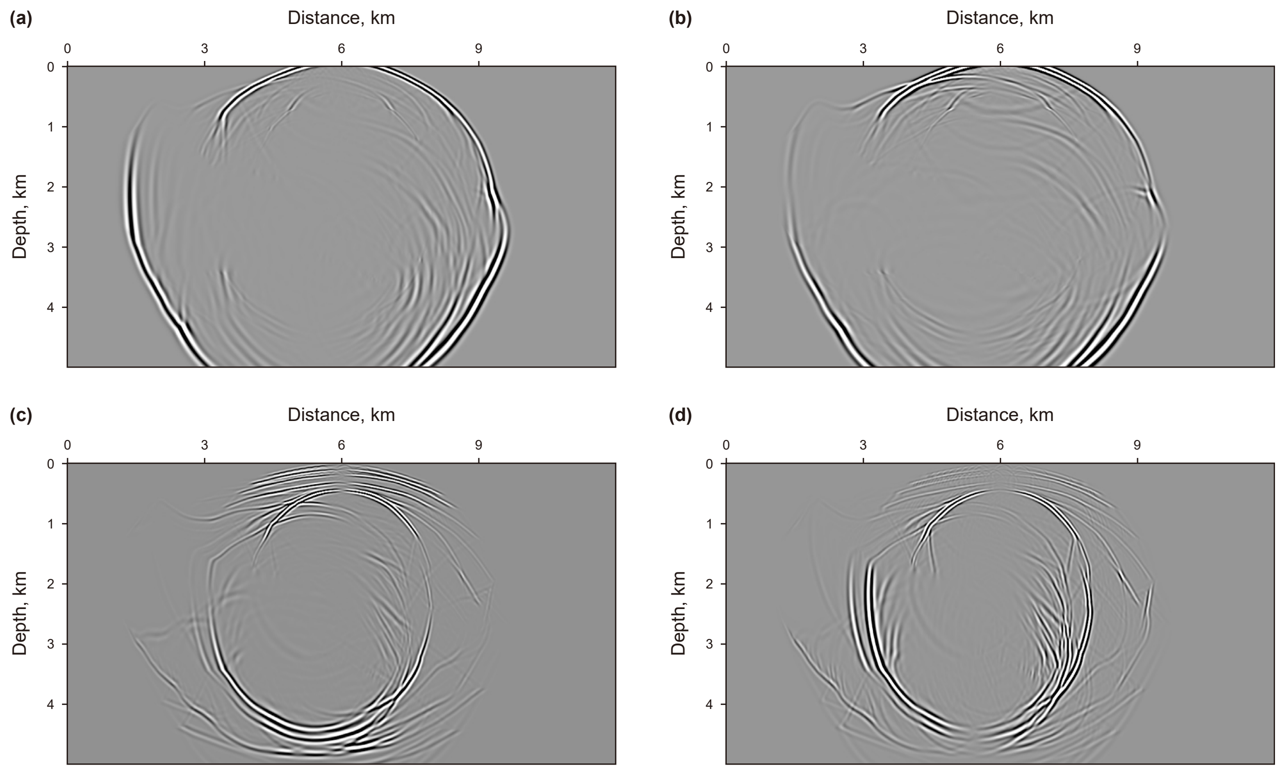

Fig. 9. The decomposed P-wave **(a)** x- and **(b)** z-components, and S-wave **(c)** x- and **(d)** z-components for the VTI Hess model at propagating time 1.2 s.

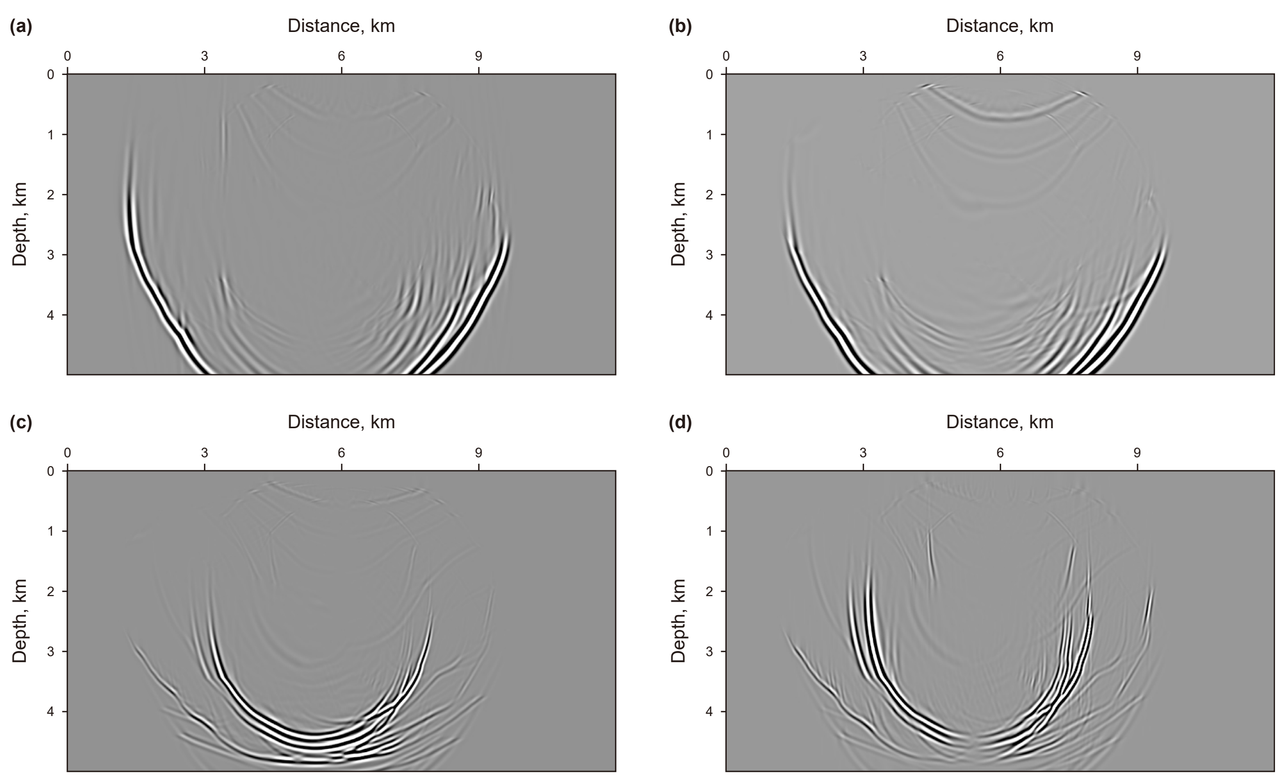

Fig. 10. The separated down-going P-wave **(a)** x- and **(b)** z-components, and down-going S-wave **(c)** x- and **(d)** z-components for the VTI Hess model at propagating time 1.2 s.

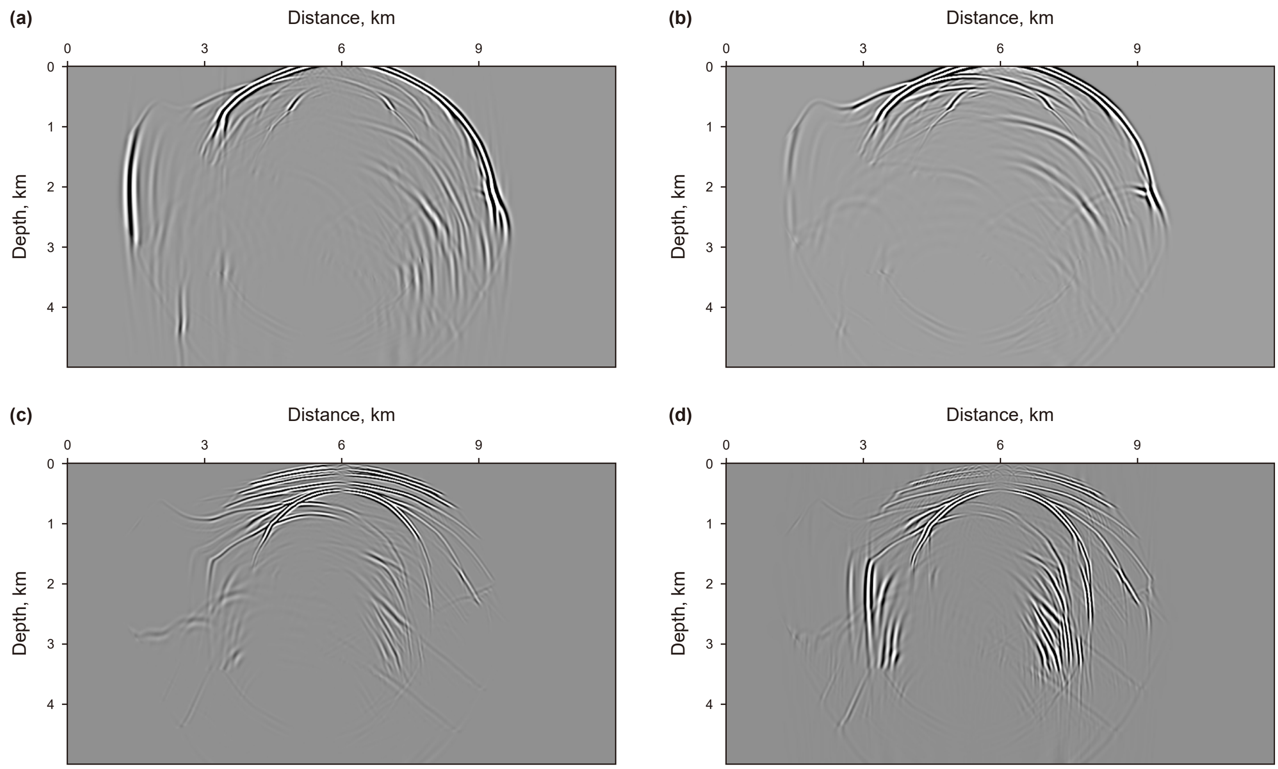

Fig. 11. The separated up-going P-wave **(a)** *x*- and **(b)** *z*-components, and up-going S-wave **(c)** *x*- and **(d)** *z*-components for the VTI Hess model at propagating time 1.2 s.

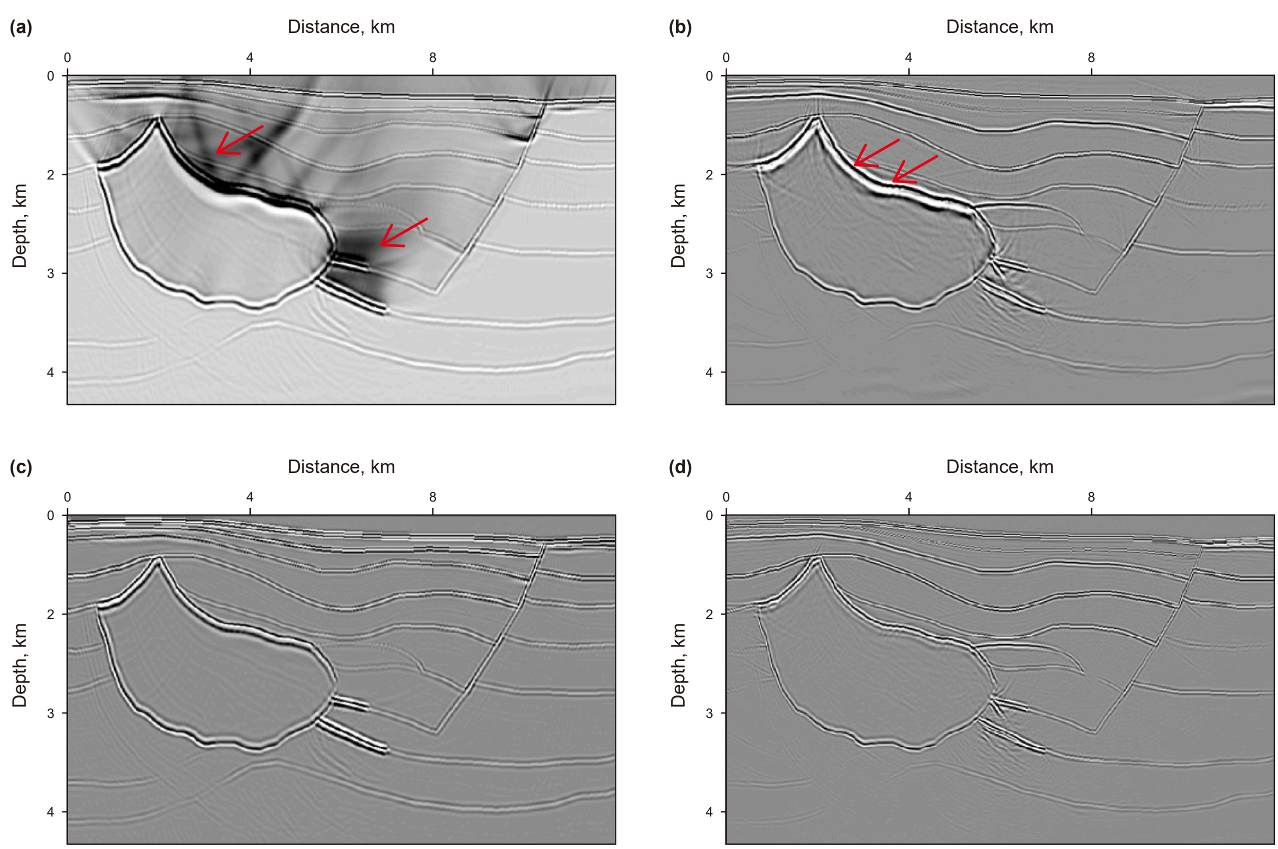

Fig. 12. ERTM image of VTI Hess model with different imaging methods. **(a)** PP- and **(b)** PS-image with conventional cross-correlation imaging condition, **(c)** PP- and **(d)** PS-image with up/down wavefield separation imaging condition.

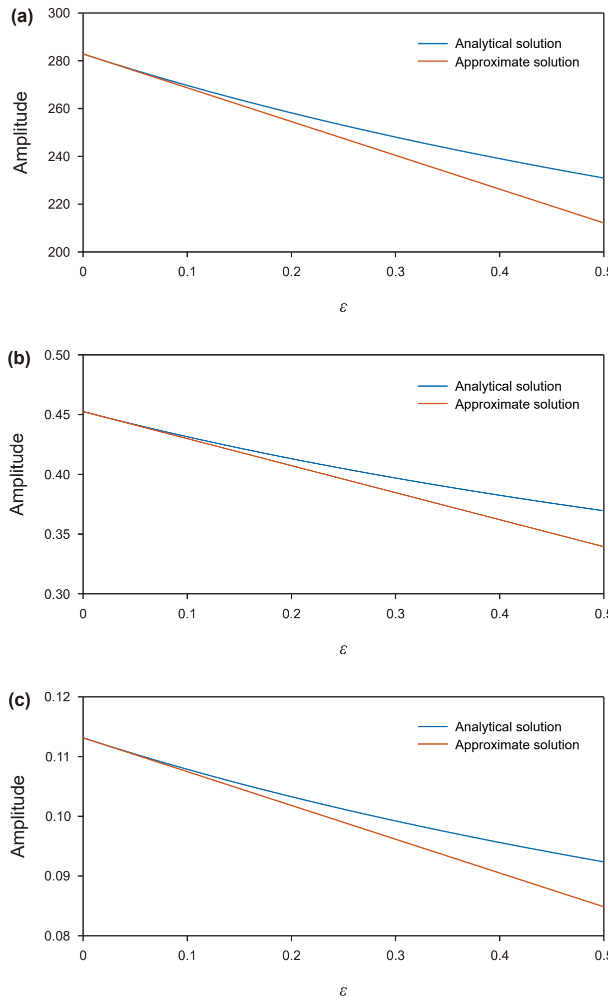

Fig. 13. Comparison of analytical (Eq. (12a)) and approximate solution (Eq. (13a)) with variation of epsilon ϵ ranging from 0 to 0.5. P-wave velocity is 2500 m/s and main frequency is 15 Hz, wavenumber components are set as **(a)** $k_x = k_z = 0.001$, **(b)** $k_x = k_z = 0.025$ and **(c)** $k_x k_z = 0.05$. Blue line denotes analytical solution and red line represents approximate solution.

6. Conclusion

We first develop an efficient P/S wave-mode decomposition of pure space domain in elastic VTI media which produces vector P- and S-wave with correct travel time and approximated amplitude, reducing cross-talk artifacts in elastic image. To further suppress the low-frequency and false images, we propose an up/down wavefield separation approach for P/S waves in elastic VTI media. Our approach solves wave equation only once and is embedded into decomposing P/S wave-mode formulation. Finally an up/down and P/S decomposition method is presented to improve the image quality of ERTM in VTI media. Simple and complex examples demonstrate the effectiveness of our approaches.

CRediT authorship contribution statement

Wei Wu: Writing – original draft, Visualization, Validation, Methodology, Formal analysis, Conceptualization. **Le-Le Zhang:** Writing – review & editing, Validation, Formal analysis, Conceptualization. **Yang Zhao:** Writing – review & editing. **Yang Liu:** Writing – review & editing. **Xiao-Feng Wu:** Writing – review & editing. **Hao-Huan Fu:** Writing – review & editing.

Declaration of competing interest

No potential conflict of interest was reported by the authors.

Acknowledgement

We appreciate the help of the editors and the anonymous reviewers for their comments and suggestions. These significantly improved the quality of this paper. This study is jointly supported by BGP. Inc, CNPC under grant 2023ZZ05-05.

References

Baysal, E., Kosloff, D.D., Sherwood, J.W.C., 1984. A two-way nonreflecting wave equation. Geophysics 49 (2), 132–141. https://doi.org/10.1190/ 1.1441644.

Caldwell, J., 1999. Marine multicomponent seismology. The Leading Edge 18, 1274–1282. https://doi.org/10.1190/1.1438198.

Cheng, J., Fomel, S., 2014. Fast algorithms for elastic-wave-mode separation and vector decomposition using low-rank approximation for anisotropic media. Geophysics 79 (4), C97–C110. https://doi.org/10.1190/geo2014-0032.1.

Dellinger, J., Etgen, J., 1990. Wave-field separation in two-dimensional anisotropic media. Geophysics 55 (7), 914–919. https://doi.org/10.1190/1.1442906.

Fan, N., Xie, X.-B., Zhao, L.-F., Yao, Z.-X., 2024. The qP- and qSV-wave separation in 2D vertically transversely isotropic media and their applications in elastic reverse time migration. Geophysics 89 (5), C211–C223. https://doi.org/10.1190/geo2023-0692.1.

Fang, X., Yao, G., Zheng, Q., Zhang, P., Wu, D., Niu, F., 2025. Fast P/S wavefield decomposition for vertical transverse isotropic media based on wavefront phase direction. Chinese. J. Geophys. 68, 1472–1486. https://doi.org/10.6038/cjg2024S0397 (in Chinese).

Fang, X.-Y., Yao, G., Zheng, Q.-Q., Zhang, P.-M., Wu, D., Niu, F.-L., 2024. Helmholtz decomposition with a scalar poisson equation in elastic anisotropic media. Pet. Sci. 21 (3), 1597–1610. https://doi.org/10.1016/j.petsci.2023.12.007.

Fei, T.W., Luo, Y., Qin, F., 2014. An endemic problem in reverse-time migration. SEG Technical Program Expanded Abstracts 2014, pp. 3811–3815. https://doi.org/10.1190/segam2014-0209.1.

Fei, T.W., Luo, Y., Yang, J., Liu, H., Qin, F., 2015. Removing false images in reverse time migration: The concept of de-primary. Geophysics 80 (6), S237–S244. https://doi.org/10.1190/geo2015-0289.1.

Granli, J.R., Arntsen, B., Sollid, A., Hilde, E., 1999. Imaging through gas-filled sediments using marine shear-wave data. Geophysics 64 (3), 668–677. https://doi.org/10.1190/1.1444576.

Liu, F., Zhang, G., Morton, S.A., Leveille, J.P., 2011. An effective imaging condition for reverse-time migration using wavefield decomposition. Geophysics 76 (1), S29–S39. https://doi.org/10.1190/1.3533914.

Liu, L., 2019. Improving seismic image using the common-horizon panel. Geophysics 84 (5), S449–S458. https://doi.org/10.1190/geo2018-0656.1.

Liu, Y.-H., Huang, J.-P., Chen, L., Mao, Q., Tian, K., 2024. 3D reverse-time migration for pure p-wave in orthorhombic media. Pet. Sci. 21 (6), 3937–3950. https://doi.org/10.1016/j.petsci.2024.07.010.

Lu, Y., Liu, Q., Zhang, J., Yang, K., Sun, H., 2019. Poynting and polarization vectors based wavefield decomposition and their application on elastic reverse time migration in 2D transversely isotropic media. Geophys. Prospect. 67, 1296–1311. https://doi.org/10.1111/1365-2478.12777.

Morse, P.M., Feshbach, H., 1953. Methods of Theoretical Physics. McGraw-Hill Book Comp., Inc.

Revelo, D.E., Pestana, R.C., 2019. Up/down acoustic wavefield decomposition using a single propagation and its application in reverse time migration. Geophysics 84 (4), S341–S353. https://doi.org/10.1190/geo2018-0305.1.

Shen, P., Albertin, U., 2015. Up-down separation using Hilbert transformed source for causal imaging condition. In: SEG Technical Program Expanded Abstracts, pp. 4175–4179.

Sun, R., Chow, J., Chen, K., 2001. Phase correction in separating P- and S-waves in elastic data. Geophysics 66 (5), 1515–1518. https://doi.org/10.1190/1 .1487097.

Tang, J., Yue, H., Xu, X., Tinnin, J., Hallin, J., 2009. Application of converted-wave 3D/3-C data for fracture detection in a deep tight-gas reservoir. The Leading Edge 28, 826–837. https://doi.org/10.1190/geo2018-0305.1.

Thomsen, L., 1986. Weak elastic anisotropy. Geophysics 51 (10), 1954–1966. https://doi.org/10.1190/1.1442051.

Tsvankin, I., 2012. Seismic Signatures and Analysis of Reflection Data in Anisotropic Media, third ed. Society of Exploration Geophysicists.

Wang, W., Hua, B., Mcmechan, G.A., Duquet, B., 2018. P and S decomposition in anisotropic media with localized low-rank approximations. Geophysics 83 (1), C13–C26. https://doi.org/10.1190/geo2017-0138.1.

Wang, W., McMechan, G.A., Tang, C., Xie, F., 2016. Up/down and P/S decompositions of elastic wavefields using complex seismic traces with applications to calculating Poynting vectors and angle-domain common-image gathers from reverse time migrations. Geophysics 81 (4), S383–S398. https://doi.org/10.1190/geo2015-0704.1.

Yan, J., Sava, P., 2009. Elastic wave-mode separation for VTI media. Geophysics 51 (10), 1954–1966. https://doi.org/10.1190/1.3184014.

Yang, J., Zhang, H., Zhao, Y., Zhu, H., 2019. Elastic wavefield separation in anisotropic media based on eigenform analysis and its application in reverse-time migration. Geophys. J. Int. 217, 1290–1313. https://doi.org/10.1093/gji/ggz085.

Yang, J., Zhu, H., Wang, W., Zhao, Y., Zhang, H., 2018. Isotropic elastic reverse time migration using the phase- and amplitude-corrected vector P- and S-wavefields. Geophysics 83 (6), S489–S503. https://doi.org/10.1190/geo2018-0023.1.

Yao, G., Fang, X., Zheng, Q., Wu, D., Niu, F., 2024. Pseudo-helmholtz decomposition for an elastic vti wavefield based on wavefront phase direction. Geophysics 89 (3), T151–T162. https://doi.org/10.1190/geo2023-0574.1.

Yu, P., Geng, J., Wang, C., 2016. Separating quasi-P-wave in transversely isotropic media with a vertical symmetry axis by synthesized pressure applied to ocean-bottom seismic data elastic reverse time migration. Geophysics 81 (6), C295–C307. https://doi.org/10.1190/geo2016-0108.1.

Zhang, L., Liu, L., Niu, F., Zuo, J., Shuai, D., Jia, W., Zhao, Y., 2022a. A novel and efficient engine for P-/S-wave-mode vector decomposition for vertical transverse isotropic elastic reverse time migration. Geophysics 87 (4), S185–S207. https://doi.org/10.1190/geo2021-0609.1.

Zhang, L., Liu, Y., Jia, W., Wang, J., 2021. Suppressing residual low-frequency noise in VSP reverse time migration by combining wavefield decomposition imaging condition with Poynting vector filtering. Explor. Geophys. 52 (2), 235–244. https://doi.org/10.1080/08123985.2020.1804298.

Zhang, L., Zhao, Y., Liu, L., Chen, K., Wang, Y., Zuo, J., 2023a. A fast anisotropic decoupled operator of elastic wave propagation in the space domain for P-/S-wave-mode decomposition and angle calculation, with its application to elastic reverse time migration in a TI medium. Geophysics 88 (3), T151–T164. https://doi.org/10.1190/geo2022-0477.1.

Zhang, L.-L., Zhao, Y., Liu, L., Chen, K., Zuo, J.-H., Wang, Y.-X., Yang, J.-D., 2023b. Extracting angle-domain common-image gathers in VTI media using ansiotropic-Helmholtz P/S wave-mode decomposition. Pet. Sci. 20 (3), 1546–1561. https://doi.org/10.1016/j.petsci.2023.02.021.

Zhang, Y., Sun, J., 2009. Practical issues of reverse time migration: true-amplitude gathers, noise removal and harmonic-source encoding. ASEG Extended Abstracts 2009.

Zhang, P., Wu, R.-S., Han, L.-G., Hu, Y., 2022b. Elastic direct envelope inversion based on wave mode decomposition for multi-parameter reconstruction of strong-scattering media. Pet. Sci. 19 (5), 2046–2063. https://doi.org/10.1016/j.petsci.2022.05.007.

Zhang, Q., McMechan, G.A., 2010. 2D and 3D elastic wavefield vector decomposition in the wavenumber domain for vti media. Geophysics 75 (3), D13–D26. https://doi.org/10.1190/1.3431045.

Zhang, Y., Zhang, G., 2009. One-step extrapolation method for reverse time migration. Geophysics 74 (4), A29–A33. https://doi.org/10.1190/1.3123476.

Zhao, Y., Zhang, H., Liu, H., Zhang, D., Sengupta, M., 2018a. Target-oriented diversity stacking for virtual-source imaging and monitoring. Lead. Edge 37 (10), 764–773. https://doi.org/10.1190/tle37100764.1.

Zhao, Y., Zhang, H., Yang, J., Fei, T., 2018b. Reducing Artifacts of Elastic Reverse Time Migration by the Deprimary Technique: Geophysics, vol. 83, pp. S569–S577.

Zheng, Q., Yao, G., 2023. An improved elastic wavefield separation method based on the helmholtz decomposition. Geophysics 88, T203–T210. https://doi.org/10.1190/geo2022-0628.1.

Zhou, X.-Y., Chang, X., Wang, Y.-B., Wen, X.-T., You, J.-C., Sun, C., 2022. Non-artifact vector P- and S-wave separation for elastic reverse time migration. Pet. Sci. 19 (6), 2695–2710. https://doi.org/10.1016/j.petsci.2022.08.006.

Zhu, H., 2017. Elastic wavefield separation based on the helmholtz decomposition. Geophysics 82, S173–S183. https://doi.org/10.1190/geo2016-0419.1.